ARTICLES
PUBLISHED ONLINE: 28 SEPTEMBER 2015 | DOI: 10.1038/NNANO.2015.202
nature nanotechnology

Surface imaging beyond the diffraction limit with optically trapped spheres

Lars Friedrich[1,2] and Alexander Rohrbach[1,3]*

Optical traps play an increasing role in the bionanosciences because of their ability to apply forces flexibly on tiny structures in fluid environments. Combined with particle-tracking techniques, they allow the sensing of miniscule forces exerted on these structures. Similar to atomic force microscopy (AFM), but much more sensitive, an optically trapped probe can be scanned across a structured surface to measure the height profile from the displacements of the probe. Here we demonstrate that, by the combination of a time-shared twin-optical trap and nanometre-precise three-dimensional interferometric particle tracking, both reliable height profiling and surface imaging are possible with a spatial resolution below the diffraction limit. The technique exploits the high-energy thermal position fluctuations of the trapped probe, and leads to a sampling of the surface 5,000 times softer than in AFM. The measured height and force profiles from test structures and *Helicobacter* cells illustrate the potential to uncover specific properties of hard and soft surfaces.

More than a dozen different scanning probe microscopy (SPM) techniques, among which the most prominent are the atomic force microscope (AFM) and the scanning tunnelling microscope (STM), illustrate the enormous demand for imaging surfaces with many and various structures, features and functions, both in technology and in nature[1–3]. To extract most efficiently reliable information from a specimen's surface as to its topography, charge, viscoelasticity and/or biochemical specificity, the interaction process between the functionalized probe and the surface needs to be optimized. In a typical SPM experiment a fine tip is scanned point wise and line wise across a surface characterized by a spatially varying charge density (STM), height profile (AFM)[4] and/or spatially varying specific interaction strength (AFM)[5] to generate a map of features $h(x,y)$. In AFM, the tip of the cantilever can only be a few nanometres in diameter, which results in spatial resolutions far beyond the optical resolution limit, which is about $\lambda/2 \approx 250$ nm at a wavelength of $\lambda = 0.5$ μm. However, especially in the biological sciences, the force of the tip $F_{tip}(x,y) \approx \kappa_{AFM} h(x,y)$ exerted on the specimen, even by soft AFM cantilevers, is too high to avoid damaging the surfaces of cells, organelles or macromolecules. Commercially available cantilevers[6] provide spring constants with a lower limit of approximately $\kappa_{AFM} \approx 10^{-2}$ N m^{-1} = 10 pN nm^{-1}, which results in large tip forces that can produce surface scratches in the AFM contact mode. In the AFM tapping mode the tip is only briefly in contact with the surface, which even allows a map of the surface of macromolecules[7]. However, the measured height profiles $h(x,y)$ depend on the applied contact force and the indentation into the soft surface[7]. Furthermore, the cantilever stiffness cannot be varied without exchanging the cantilever, which further limits the handling and accessibility of many samples because of the mechanical connection of the cantilever to the AFM frame.

However, by using an optical trap as a force transducer, the trap stiffness, κ_{OT}, can be varied easily with the laser power to achieve values 100–1,000 times smaller than a typical AFM stiffness, κ_{AFM}. This idea, already pointed out in 1992[8], allows a much gentler sampling of the object, which is more adequate for the soft structures found in cells and tissue. There followed further variations and improvements in the scanning and position tracking of the trapped probe, and also variations of the probe size and shape[9–13]. The idea of a photonic force microscope (PFM) similar to an AFM became manifest. However, some additional problems were involved: first, the thermal position fluctuations of the trapped probes, much stronger than in AFM, reduce the contact to the sample surface; and second, the optical tracking of the probe, especially in the important axial direction, becomes more complicated when the tracking light is also scattered at the sample. Therefore, in none of the studies[9–13] could the measured height profile be verified. In addition, the lateral resolution was worse than that of a conventional optical image because the probes were too large.

Nonetheless, a few years later some principal advances were achieved; for example, a weakly scattering surface of filaments from an agarose gel was imaged in three dimensions (3D)[14] by exploiting thermal position fluctuations of the trapped probe and fast 3D back-focal plane (BFP) interferometric tracking with forward-scattered light[15]. BFP interferometry in combination with quadrant photodiodes (QPDs) turned out to be the best technique for lateral and axial tracking of small and fast position changes of a trapped probe connected to single molecules[16–18] or even of deforming structures[19]. By considering multiple interferences, nanometre-precise and microsecond-fast 3D BFP interferometry[20–23] also enabled probe tracking behind surface structures that scatter the tracking light[24]. Only recently was the unconventional way of surface imaging from the side pursued by using complexly shaped probes controlled by holographic optical traps[25–27] and video tracking. Other inspiring approaches that exploit nonlinear optical effects with elongated probes[28] still need to prove their applicability for 2D surface scanning.

However, in the more than 20 years after the first proof-of-principle experiments on surface profiling with optically trapped probes[8], a robust and precise SPM technique that simply used a small trapped sphere had not been realized. In this paper, we present such a scanning probe technique that provides reliable height profiles with a lateral resolution clearly beyond the optical diffraction limit.

[1]Laboratory for Bio- and Nano-Photonics, Department of Microsystems Engineering – IMTEK, University of Freiburg, 79110 Freiburg, Germany. [2]Leica Microsystems CMS GmbH, 68165 Mannheim, Germany. [3]BIOSS Centre for Biological Signalling Studies, University of Freiburg, 79104 Freiburg, Germany. *e-mail: rohrbach@imtek.de

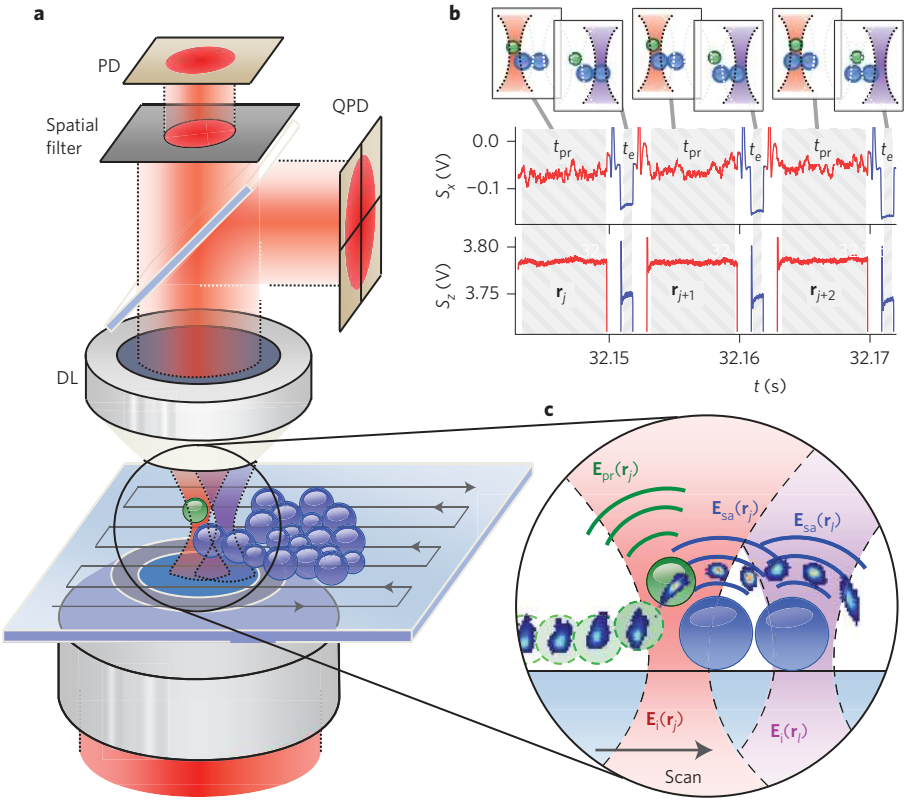

Figure 1 | Dual-beam scanning process. a, An optically trapped probe (green sphere) is moved across a sample (blue spheres). Owing to surface forces the probe is displaced from its stable trapping position and samples the height profile of the surface structure (see **c**). A detection lens (DL) captures the forward-scattered light and the unscattered light. The interference pattern of the two fields is spatially filtered and analysed with a QPD and a photodiode (PD) to track the position of the probe. **b**, The trap is held at every scan position $\mathbf{r}_j$ for a time t_{pr} so that the fluctuations of the probe can be recorded (red). Before the probe is moved to the next scan position (magenta), the focus is pointed to a different position $\mathbf{r}_j$ for a short time t_e to sample the scattering of the surface structure without hitting the probe. **c**, The two foci with and without the probe, as well as the incident fields $\mathbf{E}_i$ and the scattered fields $\mathbf{E}_{pr}$ and $\mathbf{E}_{sa}$. Differently shaped position histograms indicate the fluctuations of the probe at each beam position.

Dual-beam PFM

Typically, a PFM is designed such that the trapping laser and the tracking laser are the same. This combination of optical trapping with BFP interferometric tracking is advantageous because it reduces costs, adjustment errors and adjustment time. The usage of stabilized near-infrared lasers (see Supplementary Section 1 and Rohrbach *et al.*[22]) even allows us to distinguish small intensity changes on the QPD because of the probe displacements from unwanted laser power fluctuations[23]. The principle of BFP tracking is described next.

Probe tracking by interference signals. In regular BFP interferometry, the 3D displacement $\mathbf{b}_{pr} = (b_x, b_y, b_z)$ (pr, probe) of an optically trapped spherical probe from its equilibrium position inside the trap is tracked by recording the time-variant interference of the incident electric field $\mathbf{E}_i$ and the field $\mathbf{E}_{pr}(\mathbf{b}_{pr})$ scattered at the probe at position $\mathbf{b}_{pr}$. This interference intensity $\tilde{I}(\mathbf{k}, \mathbf{b}_{pr}) = |\tilde{\mathbf{E}}_i(\mathbf{k}) + \tilde{\mathbf{E}}_{pr}(\mathbf{k}, \mathbf{b}_{pr})|^2$ is measured with one or two QPDs located in the BFP of a detection lens (DL) or a conjugate plane thereof (Fig. 1a and Supplementary Fig. 1). In this plane, the fields are distributed according to their angular spectrum representation, $\tilde{\mathbf{E}}_i(\mathbf{k})$ and $\tilde{\mathbf{E}}_{pr}(\mathbf{k})$, $\mathbf{k} = (k_x, k_y)$. The QPD acts as an adjustable spatial filter $\mathbf{T}(\mathbf{k})$ if it is smaller than the beam diameter in the BFP. A triplet of position signals $(S_x, S_y, S_z)(\mathbf{b}_{pr}) = \iint \tilde{I}(\mathbf{k}, \mathbf{b}_{pr})\mathbf{T}(\mathbf{k})\mathrm{d}k_x\mathrm{d}k_y$ is generated and $\mathbf{b}_{pr}$ can be inferred from the signals (see Supplementary Section 1 for $\mathbf{T}(\mathbf{k})$).

However, moving a probe trapped in a focused laser beam over a structured surface (sample, sa) at position $\mathbf{b}_{sa}$ produces additional light scattering described by the electric field $\mathbf{E}_{sa}$. This leads to a three-field interference intensity $\tilde{I}_{PS}(\mathbf{b}_{pr}, \mathbf{b}_{sa}) = |\tilde{\mathbf{E}}_i + \tilde{\mathbf{E}}_{pr}(\mathbf{b}_{pr}) + \tilde{\mathbf{E}}_{sa}(\mathbf{b}_{sa})|^2$ (PS, probe scan) and therewith to incorrect position signals and incorrect surface profiles[24]. This problem can be resolved by scanning the surface with our novel dual-beam approach: as the first beam moves across the sample with the trapped probe, the second beam moves without any probe (Supplementary Movie 1). The first beam produces a space-dependent three-beam interference, which results in a signal map $\mathbf{S}_{PS}(x,y) = \iint_{BFP} \tilde{I}_{PS}(x,y,\mathbf{k})\mathbf{T}(\mathbf{k})\,\mathrm{d}^2k$, and the second beam, the 'empty beam', scatters only at the sample to provide a two-beam interference $|\tilde{\mathbf{E}}_i + \tilde{\mathbf{E}}_{sa}(\mathbf{b}_{sa})|^2$, which results in a second signal map, $\mathbf{S}_{ES}(x,y)$ (ES, empty scan). The axial components of these two signal maps are shown in pseudocolours in Fig. 2e,f with the corresponding beam arrangement sketched in Fig. 2b,c.

Structural information in the signal difference. By simply subtracting the two-beam interference signal $\mathbf{S}_{ES}(x,y)$ from the three-beam interference signal $\mathbf{S}_{PS}(x,y)$ according to equation (1), we eliminate the interferences with the light scattered at the sample to a good approximation[24]. The remaining interference between the incident light and light scattered at the probe is linear with the probe position $\mathbf{b}_{pr}$ and encodes a surface image of the sample. Scaling the difference $\mathbf{S}_{PS}(x,y) - \mathbf{S}_{ES}(x,y)$ with the detector sensitivity g (see detector calibration in Supplementary Section 3) yields the displacements $\mathbf{b}_{pr}$ of the probe relative to the trap centre:

$$\mathbf{b}_{pr} = g^{-1} \iint_{A(\mathrm{QPD})} \Big(\underbrace{\left|\tilde{\mathbf{E}}_i + \tilde{\mathbf{E}}_{pr} + \tilde{\mathbf{E}}_{sa}\right|^2}_{\text{Beam 1: probe scan}} - \underbrace{\left|\tilde{\mathbf{E}}_i + \tilde{\mathbf{E}}_{sa}\right|^2}_{\text{Beam 2: empty scan}} \Big) \mathbf{T}\mathrm{d}A \qquad (1)$$

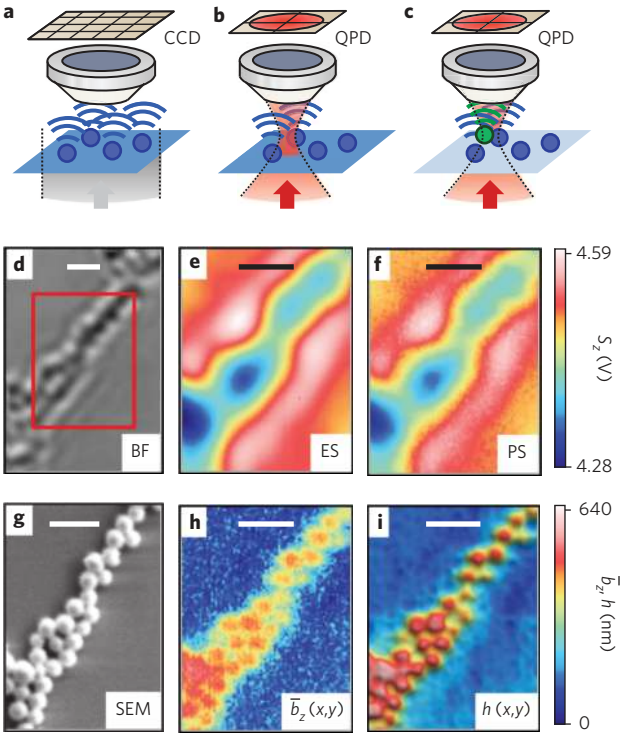

Figure 2 | Scanning results. A polystyrene probe with a 190 nm diameter is scanned across fixed silica beads with diameters of 280–500 nm. **a–c**, Sketches of BF imaging (**a**), ES (**b**) and PS (**c**). **d–f**, BF image of the scanned region (**d**), axial signal S_z recorded during ES (**e**) and axial signal S_z recorded during PS (**f**). **g–i**, SEM of the scanned region (**g**), mean axial displacements $\bar{b}_z(x,y)$ (**h**) and reconstructed height profile $h(x,y)$ (**i**). Scale bars, 1 μm.

$\mathbf{b}_{pr}(t)$ represents the 3D probe position, which changes in time because of thermal noise. After time averaging at each sample point (x,y) over a few milliseconds, a coarse surface image according to the mean axial displacement $\bar{b}_z(x,y)$ is obtained.

The suitability and reliability of this approach for surface-height profiling was tested by scanning a 190 nm polystyrene probe across an arrangement of silica spheres with diameters of 280–500 nm attached to a glass substrate. The trapping wavelength was 1,064 nm and a water-immersion lens with numerical aperture NA = 1.2 was used. The resulting surface image is shown in Fig. 2h and is compared to a regular bright-field (BF) image (Fig. 2d) and to an image obtained by scanning electron microscopy (SEM) (Fig. 2g). The BF image was taken with partially coherent light at half the wavelength (see the sketch in Fig. 2a). The structures can barely be resolved because of the multiwave interference and diffraction (at a pixel size of 100 nm). By inspecting Fig. 2e,f (pixel size 40 nm), it first appears rather unintuitive that from a simple time-averaged signal difference ($S_{PS} - S_{ES}$) a super-resolved image of the surface structure with height information is obtained. None of the structures with extents down to $\lambda_{IR}/4$ can be resolved in either the signal map of S_{ES} (Fig. 2e) or that of S_{PS} (Fig. 2f), whereas in ($S_{PS} - S_{ES}$)—although noisy—all the structures can be separated and their sizes estimated. The noise arises from the limited number of positions $\mathbf{b}_{pr}$ of the fluctuating probe at each trap position (x,y). The signals $\mathbf{S}_{PS}$ and $\mathbf{S}_{ES}$ are typically of similar strength because most light is scattered at the sample and only little light is scattered at the small probe trapped behind the focus, that is $|\tilde{\mathbf{E}}_{pr}| \ll |\tilde{\mathbf{E}}_{sa}|$.

Asymmetric switching between both beams. As the probe beam and the empty beam (indicated in Fig. 1 in red and purple, respectively) cannot be at the same surface position (x,y) at the same time, the two beams are slightly displaced in space and time during the meander-like scan across the sample. The two beams, displaced by 2 μm to each other, are time multiplexed by galvanometric scan mirrors and are then moved in an optimized jump pattern between the probe beam position $\mathbf{r}_j$ and empty beam position $\mathbf{r}_l$ (see Supplementary Figs 5 and 6 and Supplementary Movie 2). The switching between both beams is illustrated in Fig. 1b by the sketches and the position signals $S_x(t)$ and $S_z(t)$ for lateral and axial displacements. During the short resting time, $t_e \approx 1$ ms, the QPDs can collect enough interference photons scattered at the resting sample alone. The time t_e is too short for the freely diffusing probe to escape from the optical trapping potential of the probe beam.

Probe fluctuations encode the surface structure

In the following we explain how the surface profile can be uncovered from the centre positions of the fluctuating sphere.

Extracting high-energy fluctuations. During the resting time of the probe beam, $t_{pr} \approx 8$ ms, the spherical probe diffuses inside the trapping potential to explore its volume several times. The autocorrelation time, which is the time the probe needs to explore its harmonic potential, is about $t_{pr}/8$ in the axial and about $t_{pr}/50$ in the lateral direction. At each beam position $\mathbf{r}_j$, 800 3D positions of the probe are recorded with nanometre precision at 100 kHz. The positions are combined to give a 3D histogram for each scan point j with a sampling distance $|\mathbf{r}_j - \mathbf{r}_{j+1}| = 40$ nm.

Figure 1c shows a sequence of 2D position histograms of the probe (green sphere) undergoing Brownian motion. The position histograms become displaced and deformed by the sample (blue spheres) when the probe is moved across them. The closer the probe and the sample come, the more deformed are the position histograms. Only the probe fluctuations with high fluctuation energies towards the sample enable the probe to contact the surface, and hence can be selected to recover a reliable height profile of the surface[14]. This energy selection is possible because of the high bandwidth of the interferometric tracking system, which results in a resolution of the position histograms $p(\mathbf{r})$ and energy histograms $W(\mathbf{r}) = -k_B T \ln(p(\mathbf{r}))$ of only a few nanometres ($k_B T \approx 4 \times 10^{-21}$ J is the thermal energy). Here probe diffusion in thermal equilibrium and Boltzmann statistics were assumed. By considering only these high-energy probe fluctuations, a super-resolution image with high contrast (Supplementary Fig. 9), little noise and an additional height profile can be obtained, as shown in Fig. 2i.

Convolution of position histogram and probe geometry. The structure presented in Fig. 2 was scanned over an area of 3 × 4 μm discretized into $N = 3 \times 4$ μm$/\delta r = 7{,}500$ sample points in a distance between points of $\delta r = 40$ nm, which results in N mean positions $\bar{b}_z$ and N position histograms $p_j(\mathbf{r})$. The N histograms are combined into a large histogram of all the probe centre positions $p(\mathbf{r})$, as indicated in Fig. 3b–d by the bluish dot distribution of the cross-sections $p(y,z)$ and $p(x,z)$. They correspond to the line scans numbered 1, 2 and 3 as indicated in Fig. 3a, which presents the height profile $h(x,y)$ that corresponds to the structure in Fig. 2h. In the axial z-direction, the probe's fluctuations are limited by the optical trapping potential $W_{opt}(\mathbf{r})$ on the upper side and by the repulsive surface potential $W_s(\mathbf{r})$ on the lower side. Here the electrostatic screening length was tuned to be $\Lambda < 5$ nm. Accordingly, the height profile $h(x,y)$ of the sample is encoded by the lower boundary of the position distribution $p(\mathbf{r})$ of the probe. Further, the spherical probe has a finite radius, a_{pr}, so that it is not the tracked centre positions but the probe's surface that delimits the sample surface. The spherical

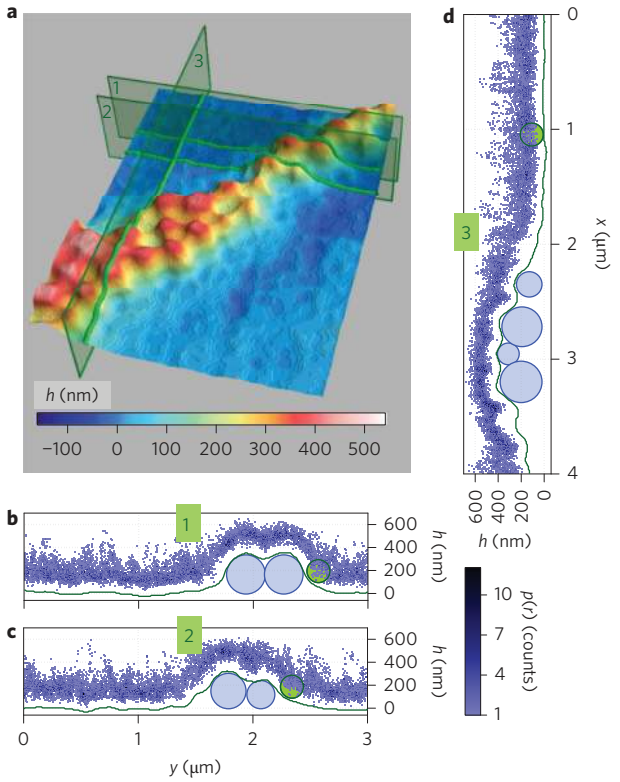

Figure 3 | Height-profile mapping. a, Three slices (1, 2 and 3) through the scan domain are illustrated by the histograms $p(x,z)$ and $p(y,z)$ of the probe centroid recorded during the scanning process. **b**–**d**, By convolution with the probe geometry (green sphere), the height profile $h(x,y)$ of the scanned sample can be obtained (shown as a surface plot in **a** and green line profiles in **b**–**d**).

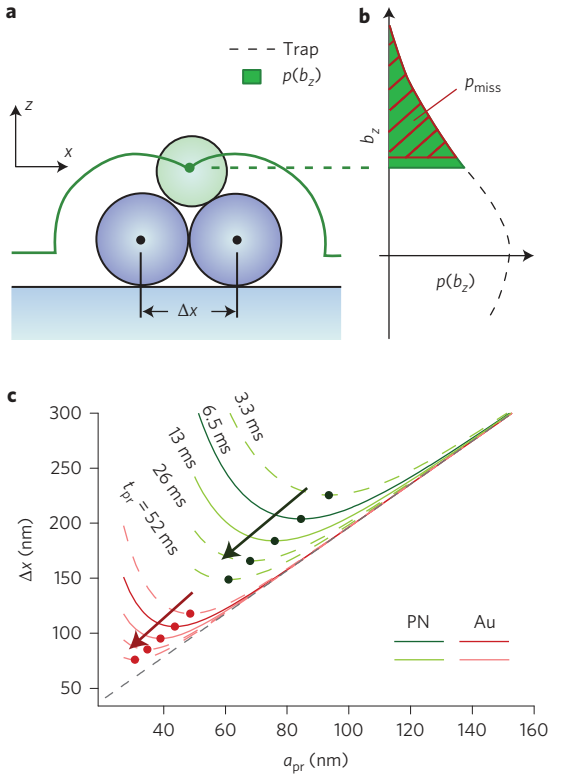

Figure 4 | Spatial image resolution. a, A structure composed of two spherical particles in a contact distance of Δx is scanned with a spherical probe of radius a_{pr}, which leads to a dip in the rollover trajectory of the probe (green curve). **b**, Probability density $p(b_z)$ to find the trapped probe at relative position b_z without (dashed line) and with (green area) the surface structure. p_{miss} describes the probability that the probe misses the dip. **c**, The resolution limit Δx for polystyrene (PN in green) and gold (Au in red) probes is given as a function of the probe radius a_{pr}. The straight dashed line is the limiting case $\Delta x \approx a_{pr}$ of no thermal fluctuations. With increasing measurement time, t_{pr}, the resolution improves (arrows). Dots indicate the minima of the theoretical curves with t_{pr} = 3.3, 6.5, 13, 26 and 52 ms.

volume of the probe ($V = 4\pi/3a_{pr}^3$) is indicated in Fig. 3b–d and can be described by a shape function $s(\mathbf{r}) = \theta(a_{pr} - |\mathbf{r}|)/V$, with unit step function $\theta(x)$. As the minimal distance between the surface of the sample and the probe centre is a_{pr}, the overall position histogram $p(\mathbf{r})$ needs to be convolved with the probe's shape function $s(\mathbf{r})$. In this way, the convolution $O(\mathbf{r}) = p(\mathbf{r}) * s(\mathbf{r})$ becomes a measure for the volume occupied by the fluctuating probe (Supplementary Fig. 7 and Supplementary Movie 3) and is linked to the governing potentials, as shown in equation (2):

$$O(\mathbf{r}) = p_0\left(\exp[-\tfrac{1}{k_B T}(W_S(\mathbf{r}) + W_{opt}(\mathbf{r}))] * s(\mathbf{r})\right) \quad (2)$$

The occupied volume $O(\mathbf{r})$ is limited by the interaction of the probe with the surface. The edge of this volume at $O(\mathbf{r}) = 0$ represents the desired surface profile. As can be seen in Fig. 3a and (and also in Fig. 6a), outliers in the position histogram become visible as spherical indentations in the reconstructed height profile. To reduce this unwanted effect, we chose $O(x,y,h(x,y)) = 0.05$ (see Supplementary equation (6)).

The described principle is well recognized in Fig. 3b–d, where the measured surface height $h(x,y)$ is at a distance of the green sphere's radius to the outermost centre positions that belong to high fluctuation energies. The effect of the convolution with the probe volume is also shown by the transition from Fig. 2h to Fig. 2i, where the corrected surface height in combination with strongly reduced noise becomes apparent. From a comparison between the height profiles shown in Fig. 2i (using a 190 nm probe) and the profiles extracted from the SEM image (Fig. 2g), we find a mean relative error of 1.6% for 20 out of 22 sample spheres, which is a very good result (Supplementary Fig. 11).

Surface-imaging results

We address the apparent questions about what kind of structures can be resolved with our technique, and what effects limit the spatial resolution.

Resolution of the surface image. The lateral resolution of the described imaging technique is defined by the smallest distance Δx of two spherical objects that appear separated in the measured height profile. As illustrated in Fig. 4a, the resolution is always limited by the probe size. However, as the optical forces scale with the probe volume, a minimal size is required for stable trapping and surface scanning. Here we also carried out the first tests with gold spheres with a diameter $2a_{pr} < 100$ nm (not shown), which produce much stronger forces than latex spheres of equal size, but reflect more light and so make position tracking more erroneous. Future investigations must show whether this effect can be compensated by a direction- and polarization-dependent detection. In addition to these geometrical constraints, there exists a probability, p_{miss}, for the thermally fluctuating probe to not visit the hollow in the surface structure during the finite tracking time t_{pr} at each trap position (see Fig. 4b). As derived in the Supplementary Information, the spatial resolution of our surface imaging technique is given by equation (3):

$$\Delta x \approx 2\,a_{pr}\left(1 + \frac{C}{a_{pr}^{4.3}(\alpha_{pr}^2 P^2 t_{pr})^{0.6}}\right) \quad (3)$$

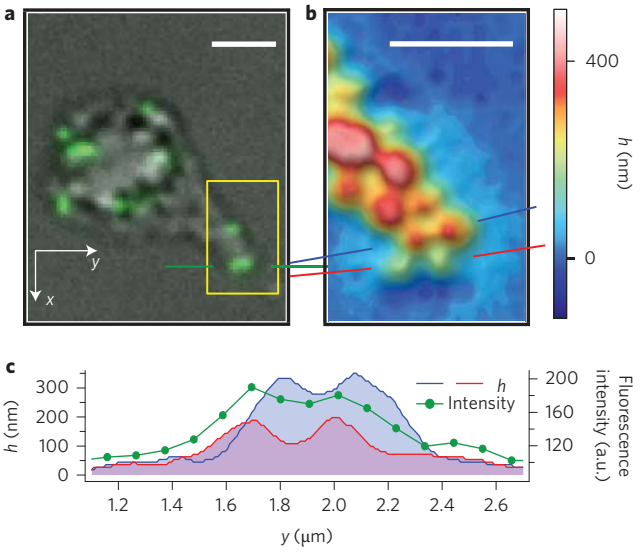

Figure 5 | Imaging different sample materials. A structure fabricated from a mixture of non-fluorescent silica beads (radius a_{sa} = 175 nm) and fluorescent polystyrene beads (a_{sa} = 100 nm) is scanned with a polystyrene probe (a_{pr} = 100 nm). **a**, Overlay of BF and epifluorescence image. **b**, Measured height profile $h(x,y)$ from the marked area in **a**. **c**, Line profiles of height profile $h(y)$ and fluorescence intensity along the green line indicated in **a** and the blue and red lines in **b**. Scale bars, 1 μm.

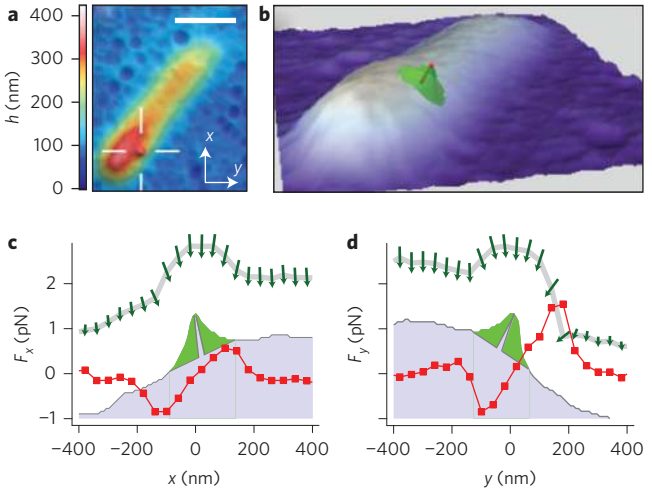

Figure 6 | Force microscopy of *H. pylori*. **a**, Height profile of a bacterium embedded in agarose gel. The profile is from a scan with a 350 nm polystyrene sphere, and the cross marks a protrusion. **b**, The magnified profile from the side reveals a protrusion (pilus) of 150 nm length and 28° vertical tilt. **c**,**d**, Lateral height profiles (shaded area) with subpiconewton forces $F_x(x)$ (**c**) and $F_y(y)$ (**d**) exerted on the surface, indicated by strength and direction (green arrows), as well as force profiles on the pilus (red lines) during a regular scan. The green-shaded area around the pilus indicates the volume not accessible by the sphere. Scale bar, 1 μm.

with the probe's polarizability α, the laser power P and constant $C = 7.2 \times 10^9\,\mathrm{mW^{1.2}\,ms^{0.6}\,nm^{4.3}}$. Figure 4c shows some typical courses of $\Delta x(a_{pr})$ for polystyrene and gold as the probe materials. It can be seen that smaller probes yield a better resolution up to the point where the probe fluctuations become dominant (minimal Δx). Typically, surfaces were scanned with speeds of 4 μm s^{-1}, which corresponds to 100 sample positions per second at a tracking time of t_{pr} = 8 ms. By increasing the tracking time t_{pr} at each scan point, the measured histograms $p_j(\mathbf{r},t_{pr})$ become more pronounced in shape and the achievable resolution could be increased further.

Imaging structures of varying size and refractive index. To prove that our SPM technique can be applied flexibly to various transparent samples, we investigated a mixture of spherical beads with different sizes and refractive indices n_{sa}. We verified the measured height profile by using non-fluorescent silica spheres (nominal diameter 350 nm, n_{sa} = 1.45) and green fluorescent polystyrene spheres (200 nm, n_{sa} = 1.57). This sample arrangement is shown in Fig. 5a by a combined BF and fluorescence image. Figure 5b depicts the height profile $h(x,y)$ measured with a 190 nm latex probe, and the two regions for the line scans through the larger non-fluorescent silica spheres (blue line) and the smaller fluorescent polystyrene spheres (red line). The profiles in Fig. 5c reveal not only the correct heights (sphere diameters), but also a better resolution and higher contrast relative to the fluorescence image shown by the intensity line scan (green line). This image was acquired by a lens with NA = 1.2 at $\lambda \approx 0.5$ μm, which in practice enables a diffraction-limited spatial resolution of $\Delta x \approx 0.3$ μm. As explained in Supplementary equation (5), the tracking precision solely depends on the scattering at the sample and cannot be increased by the probe.

Height and force profiling of a cell surface. As introduced earlier, our SPM technique works in transmission mode and therefore requires transparent samples, and most biological cells are transparent and absorb only little energy at the used wavelength of 1,064 nm. As a biological application we investigated the surface of the bacterium *Helicobacter pylori*. This bacterium is known to cause serious diseases in the human stomach, such as gastric ulcers or even cancer. On its surface it can produce pili with a length in the order of 200 nm that seem to play an important role in their pathogenesis[29]. To image the surface of this bacterium, we used a 350 nm polystyrene probe. At this probe size, the optical forces exerted by the trap with a total optical power of 60 mW are strong enough to prevent the probe from sticking (see Supplementary Section 10 for the amount of energy exposed). Figure 6a,b displays a surface image $h(x,y)$ of the bacterium in a so-far unequalled quality without the need of staining. In particular, $h(x,y)$ reveals a single protrusion, marked by a cross in Fig. 6a and enlarged in Fig. 6b. Here the uncertainty region caused by the limited accessibility of the spherical probe size is shaded in green. As the occupied volumes (equation (2)) left and right of the pilus do not overlap, a bending of the pilus during the scan can be excluded. The cross-sections of Fig. 6c,d reveal a length of 150 nm for the bacterial pilus, which is situated in a precisely measureable angle on the bacterial body. In addition, force profiles can be deduced easily from the probe's displacement from the trap centre. The green arrows in Fig. 6c,d indicate the direction and strength of the exerted surface force, whereas the red curves indicate the lateral forces, in piconewtons, applied to the pilus during a regular scan. By these lateral forces the bending stiffness of the pilus or its ability to unwind[30] can be investigated and might give new insights into their function, which is especially interesting for different cell mutants or different mechanical perturbations. Based on the principles introduced, our PFM scanning technique should also be applicable to the surfaces of cells that are several micrometres thick if the height variations are not larger than about 0.5 μm.

Conclusions

We have demonstrated that a reliably working SPM can be realized through a standard optical tweezers system that scans a simple trapped sphere across submicron-scale surface structures. By

generating a time-multiplexed twin focus and measuring the difference between the intensity signals induced in both foci, the successful concept of interferometric probe tracking can also be applied in the presence of light-scattering surface structures. Owing to the high precision and bandwidth of our tracking technique, we are able to select high-energy fluctuations of the probe to recover various surface profiles. We achieved a mean axial precision of about 6 nm, a lateral resolution increased by 50% and a superior contrast relative to those achievable with a high-end objective lens with NA = 1.2. By subsequent 40 nm displacements of the trapped dielectric spherical probe with a 95 nm radius, a transparent surface area of 1 μm² can be imaged in ten seconds. We exert extremely gentle forces in the subpiconewton range onto the surface using axial force constants of $\kappa_{OT} \approx 2 \times 10^{-6}$ N m^{-1}, which are 5,000 times smaller than those of a soft AFM cantilever. The current resolution of about one-fifth of the trapping wavelength and our estimation of the achievable resolution demonstrates the strong potential of this technique, especially if the size of the probe can be reduced further. This could be realized by increasing the optical forces using different trapping wavelengths and probe materials, surface coatings or shapes[28,31,32]. The usage of the advanced scan techniques known from AFM, such as the tapping mode, could reduce the risk of the probe sticking to the sample and could allow the mapping of viscoelastic parameters, which would give this technique a bright future in the bionanosciences.

Received 22 December 2014; accepted 10 August 2015; published online 28 September 2015

References

1. Santos, N. C. & Castahno, M. A. R. B. An overview of the biophysical applications of atomic force microscopy. *Biophys. Chem.* **107,** 133–149 (2004).
2. Somorjai, G. A. & Li, Y. Impact of surface chemistry. *Proc. Natl Acad. Sci. USA* **108,** 917–924 (2011).
3. Hoerber, J. K. H. & Miles, A. M. J. Scanning probe evolution in biology. *Science* **302,** 1002–1005 (2003).
4. Dufrene, Y. F. *et al.* Multiparametric imaging of biological systems by force–distance curve-based AFM. *Nature Methods* **10,** 847–854 (2013).
5. Dupres, V. *et al.* Nanoscale mapping and functional analysis of individual adhesins on living bacteria. *Nature Methods* **2,** 515–520 (2005).
6. Ludwig, T. *et al.* Probing cellular microenvironments and tissue remodeling by atomic force microscopy. *Pflügers Archiv Eur. J. Physiol.* **456,** 29–49 (2008).
7. Wiggins, P. A. *et al.* High flexibility of DNA on short length scales probed by atomic force microscopy. *Nature Nanotech.* **1,** 137–141 (2006).
8. Malmqvist, L. & Hertz, H. M. Trapped particle optical microscopy. *Opt. Commun.* **94,** 19–24 (1992).
9. Ghislain, L. P. & Webb, W. W. Scanning-force microscope based on an optical trap. *Opt. Lett.* **18,** 1678–1680 (1993).
10. Kawata, S., Inouye, Y. & Sugiura, T. Near-field scanning optical microscope with a laser trapped probe. *Jpn J. Appl. Phys.* **33,** L1725–L1727 (1994).
11. Florin, E.-L. *et al.* Photonic force microscope based on optical tweezers and two-photon excitation for biological applications. *J. Struct. Biol.* **119,** 202–211 (1997).
12. Sugiura, T. *et al.* Gold-bead scanning near-field optical microscope with laser-force position control. *Opt. Lett.* **22,** 1663–1665 (1997).
13. Friese, M. E. J. *et al.* Three-dimensional imaging with optical tweezers. *Appl. Opt.* **38,** 6597–6603 (1999).
14. Tischer, C. *et al.* Three-dimensional thermal noise imaging. *Appl. Phys. Lett.* **79,** 3878 (2001).
15. Pralle, A. *et al.* Three-dimensional high-resolution particle tracking for optical tweezers by forward scattered light. *Microsc. Res. Tech.* **44,** 378–386 (1999).
16. Neuman, K. C. *et al.* Ubiquitous transcriptional pausing is independent of RNA polymerase backtracking. *Cell* **115,** 437–447 (2003).
17. Bormuth, V. *et al.* Protein friction limits diffusive and directed movements of kinesin motors on microtubules. *Science* **325,** 870–873 (2009).
18. Becker, N. *et al.* Three-dimensional bead position histograms reveal single-molecule nano-mechanics. *Phys. Rev. E* **71,** 021907 (2005).
19. Koch, M. & Rohrbach, A. Object adapted optical trapping and shape tracking of energy switching helical bacteria. *Nature Photonics* **6,** 680–686 (2012).
20. Rohrbach, A., Kress, H. & Stelzer, E. H. K. Three-dimensional tracking of small spheres in focused laser beams: influence of the detection angular aperture. *Opt. Lett.* **28,** 411–413 (2003).
21. Dreyer, J. K., Berg-Sørensen, K. & Oddershede, L. B. Improved axial position detection in optical tweezers measurements. *Appl. Opt.* **43,** 1991–1995 (2004).
22. Rohrbach, A. *et al.* Trapping and tracking a local probe with a photonic force microscope. *Rev. Sci. Instrum.* **75,** 2197–2210 (2004).
23. Friedrich, L. & Rohrbach, A. Improved interferometric tracking of trapped particles using two frequency-detuned beams. *Opt. Lett.* **35,** 1920–1922 (2010).
24. Seitz, P. C., Stelzer, E. H. K. & Rohrbach, A. Interferometric tracking of optically trapped probes behind structured surfaces: a phase correction method. *Appl. Opt.* **45,** 7309–7315 (2006).
25. Phillips, D. B. *et al.* Surface imaging using holographic optical tweezers. *Nanotechnology* **22,** 285503 (2011).
26. Phillips, D. B. *et al.* An optically actuated surface scanning probe. *Opt. Express* **20,** 29679–29693 (2012).
27. Phillips, D. B. *et al.* Shape-induced force fields in optical trapping. *Nature Photonics* **8,** 400–405 (2014).
28. Nakayama, Y. *et al.* Tunable nanowire nonlinear optical probe. *Nature* **447,** 1098–1101 (2007).
29. Rohde, M. *et al.* A novel sheathed surface organelle of the *Helicobacter pylori* CAG type IV secretion system. *Mol. Microbiol.* **49,** 219–234 (2003).
30. Andersson, M. *et al.* A structural basis for sustained bacterial adhesion: biomechanical properties of CFA/I pili. *J. Mol. Biol.* **415,** 918–928 (2012).
31. Jannasch, A. *et al.* Nanonewton optical force trap employing anti-reflection coated, high-refractive-index titania microspheres. *Nature Photonics* **6,** 469–473 (2012).
32. Grießhammer, M. & Rohrbach, A. 5D-tracking of a nano-rod in a focused laser beam—a theoretical model. *Opt. Express* **22,** 6114–6132 (2014).

Acknowledgements

The authors thank M. Koch, D. Ruh, A. Seifert and T. Henze for a careful reading of the manuscript and/or for helpful discussions. We also thank B. Waidner for helping with the *H. pylori* bacteria and C. Müller for support with the SEM-image acquisition.

Author contributions

L.F. performed the experiments, analysed the data and prepared all the graphs. A.R. initiated and supervised the project. A.R. and L.F. co-wrote the manuscript.

Additional information

Supplementary information is available in the online version of the paper. Reprints and permissions information is available online at www.nature.com/reprints. Correspondence and requests for materials should be addressed to A.R.

Competing financial interests

The authors declare no competing financial interests.